8-2023

Revisiting the Diffuse Layer Polarization of a Spherical Grain in Electrolytes with Numerical Solutions of Nernst-Planck-Poisson Equations

Qifei Niu
Boise State University

This document was originally published in *JGR Solid Earth* by Wiley on behalf of the American Geophysical Union: Niu, Qifei. (2023). "Revisiting the Diffuse Layer Polarization of a Spherical Grain in Electrolytes with Numerical Solutions of Nernst-Planck-Poisson Equations". *JGR Solid Earth, 128*(8), e2022JB025934. https://doi.org/10.1029/2022JB025934

JGR Solid Earth

RESEARCH ARTICLE
10.1029/2022JB025934

Revisiting the Diffuse Layer Polarization of a Spherical Grain in Electrolytes With Numerical Solutions of Nernst-Planck-Poisson Equations

Qifei Niu[1]

[1]Department of Geosciences, Boise State University, Boise, ID, USA

Key Points:

- Polarization of the diffuse layer of grain involves both tangential and normal movements of ions within it
- Fluid salinity affects the relaxation time by changing the relative importance of normal and tangential ion fluxes
- The Fixman model is modified to describe diffuse layer polarization of grains over a broad salinity range

Supporting Information:

Supporting Information may be found in the online version of this article.

Correspondence to:

Q. Niu,
qifeiniu@boisestate.edu

Citation:

Niu, Q. (2023). Revisiting the diffuse layer polarization of a spherical grain in electrolytes with numerical solutions of Nernst-Planck-Poisson equations. *Journal of Geophysical Research: Solid Earth*, *128*, e2022JB025934. https://doi.org/10.1029/2022JB025934

Received 28 OCT 2022
Accepted 14 AUG 2023

Author Contributions:

Conceptualization: Qifei Niu
Data curation: Qifei Niu
Formal analysis: Qifei Niu
Funding acquisition: Qifei Niu
Investigation: Qifei Niu
Methodology: Qifei Niu
Project Administration: Qifei Niu
Resources: Qifei Niu
Software: Qifei Niu
Validation: Qifei Niu
Visualization: Qifei Niu
Writing – original draft: Qifei Niu
Writing – review & editing: Qifei Niu

Abstract Induced polarization (IP) has been frequently used in solid earth geophysics, hydrology, and environmental sciences. A mechanistic understanding of the IP responses of geological materials is crucial for correctly interpreting field IP measurements. In this study, the fully-coupled, nonlinear Nernst-Planck-Poisson equations are numerically solved to analyze the electrochemical mechanism of diffuse layer polarization around a spherical grain immersed in electrolytes. The numerical results show diffuse layer polarization is formed by the charge separation between counterions in the diffuse layer and charges on the grain surface. Both tangential and normal movements of counterions in the diffuse layer are involved in the polarization process, but their relative contributions are distinct. Although the normal flux of counterions outweighs the flux in the tangential direction, the latter exerts a much more profound effect on the enhanced permittivity than the former. As the salinity increases, more tangential fluxes are involved in the polarization, and a longer time is required to polarize the diffuse layer fully. Theoretical models considering either pure tangential or normal fluxes are not able to correctly describe diffuse layer polarization. The Fixman model, which considers fluxes in both directions, could accurately predict the IP responses of the grain-electrolyte system over a broad salinity range if the length parameter in the model is correctly chosen.

Plain Language Summary Geoelectrical methods have been frequently used in geophysics and hydrology to characterize subsurface lithology and monitor dynamic processes, such as groundwater circulation. The key to geoelectrical field data interpretation is a physical understanding of the electrical properties of soils and rocks. In this study, computational simulations are used to understand the effect of mineral-fluid interface on geological material's ability to store electrical energy (permittivity). The simulation results show that the movement patterns of the excess charges at the mineral-fluid interface control the permittivity of geological materials at low frequencies. In general, as the ion concentration in the fluid increases, a larger fraction of excess charges at the interface will move circumferentially around a solid grain if compared to ions moving radially. The change in movement patterns will require more time for the grain to store external electric energy. An improved theoretical model is also suggested to incorporate the microscopic scale processes better. The new model can be used to aid the data interpretation of field geoelectrical measurements in many geoscience disciplines.

1. Introduction

Induced polarization (IP) is an electric field-stimulated phenomenon in materials, and it is usually observed as either a delayed voltage response in the time domain or an enhanced permittivity at low frequencies relative to the high-frequency dielectric permittivity. In exploration geophysics, the IP method has been commonly used in the search for metallic mineral deposits (e.g., Macnae & Hine, 2016; Nelson and Van Voorhis, 1983; Revil et al., 2022; Šumi, 1961; Wu et al., 2021) due to the strong electrochemical polarization occurred at the metal-electrolyte interface (Gurin et al., 2015; Revil et al., 2015; Slater et al., 2006, 2007; Wong, 1979). In the last two decades, the IP method has been increasingly used in hydrology and environmental sciences (Kemna et al., 2012), for example, to estimate permeability (Attwa & Günther, 2013; Binley et al., 2005; Börner et al., 1996; Hördt et al., 2007; Revil & Florsch, 2010; Weller et al., 2015), characterize near-surface lithology (Gazoty et al., 2012), monitor microbial growth in porous media (Davis et al., 2006; Revil et al., 2012), delineate contaminant plumes (Deceuster & Kaufmann, 2012; Schwartz & Furman, 2012), and study clay, clay-rich rocks, and rock-water interactions (e.g., Okay et al., 2014; Mendieta et al., 2023; Halisch et al., 2018).

The low-frequency (<kHz) IP response of geological materials (without metallic grains) is associated with the electrical double layer (EDL) formed at the mineral-electrolyte interface. Most rock/soil-forming minerals are charged on the surface (e.g., due to isomorphous substitution; Schroeder, 2018). Therefore, counterions in the electrolyte will accumulate at the mineral-electrolyte interface, forming a thin layer (i.e., EDL) to shield the surface charges (e.g., Mitchell & Soga, 2005). Under an external electric field, the ionic fluxes in the EDL are not identical for cations and anions due to a higher concentration of counterions. This local-scale imbalance in ionic flux creates zones of ions accumulation and deficit (Chelidze & Gueguen, 1999), which manifest themselves as an enhanced effective permittivity of the material at low frequencies (e.g., Niu et al., 2020).

In general, the EDL-related IP responses of geological materials can be modeled with different assumptions of material microstructures (e.g., Bücker et al., 2019; Niu et al., 2020). The grain polarization model treats the materials as an assembly of discrete grains, and the induced ion deficit and accumulation zones are at the opposite sides of the grain (e.g., Lyklema et al., 1983; Schwarz, 1962). This type of model has been widely used to describe the permittivity enhancement of colloids and granular materials (e.g., Leroy et al., 2008; Lesmes & Morgan, 2001). The pore polarization model assumes that the ion deficit and accumulation zones are at the two sides of a large pore body (e.g., Niu & Revil, 2016; Niu & Zhang, 2018). Although this pore (body) polarization concept has been frequently used in modeling the IP responses of sedimentary rocks (e.g., Revil et al., 2014; Zhang et al., 2017), no rigorous theory was developed; in practice, models developed for grain polarization (e.g., Schwarz, 1962) are simply applied to pore bodies without justifications. The third concept of IP in porous media is membrane polarization, which deals with the ion accumulation and deficit across a narrow pore throat (e.g., Bücker & Hördt, 2013; Marshall & Madden, 1959; Titov et al., 2002). Recently, membrane polarization has received increased attention and its contribution to the low-frequency permittivity of sedimentary rocks has been revisited (Bairlein et al., 2016; Bücker et al., 2019; Niu et al., 2020).

The EDL has two components, the Stern layer and diffuse layer. While counterions in the Stern layer are mainly adsorbed to the mineral surface, counterions in the outer layer are relatively free, moving away from the mineral surface into the bulk solution. These two layers respond differently during polarization. It is generally assumed that the counterions in the Stern layer only move tangentially under an external electric field, and the permittivity enhancement can be described by a Debye-type model (Schwarz, 1962). In the diffuse layer, the radial or normal movement of ions is possible, and many theories have also been developed to account for its contribution to EDL polarization. Examples include the Fixman model (Fixman, 1980) and the Dukhin-Shilov model (Shilov et al., 2001). Note that existing models of diffuse layer polarization give inconsistent results in terms of both relaxation time and enhanced permittivity. It is also unclear how ions in the diffuse layer respond and communicate with bulk solutions under the external electric field. The effects of other factors, such as salinity and coions in the EDL, are also unknown for diffuse layer polarization.

The objectives of this study are (a) to better understand the ion movement during the diffuse layer polarization of spherical grains and (b) to reconcile different diffuse layer polarization models. It is challenging to theoretically analyze these problems because of the complex and coupled nature of the processes. Furthermore, direct experiment observation of ion movement may not be possible due to the small thickness (~tens of nanometers or even less) of the diffuse layer. In this study, we propose to numerically solve the Nernst-Planck-Poisson equations (e.g., Brumleve & Buck, 1978) to analyze the diffuse layer polarization of a spherical grain. The Nernst-Plank-Poisson equations can describe the spatial distributions of ion concentration and electric potential near a charged surface in a coupled fashion. Also, ionic movement in different directions in the EDL can be extracted from the numerical solutions, and thus ion dynamics during polarization can be easily tracked and quantified. Note that the ion dynamics in this study refer to a continuum-level description of ion movements here, and the movement of individual ions is not tracked. In addition, ion movement is not limited to the diffuse layer, and the exchange between EDL and the bulk solution can also be considered in the simulation. Given these advantages, using numerical solutions of Nernst-Planck-Poisson equations is an ideal means for studying the diffuse layer polarization mechanism. Recently, this numerical method has been used in rock physics, for example, to study electrode polarization (Bücker et al., 2018, 2019) and membrane polarization (Bücker et al., 2019). It should be addressed that these existing studies only solved the linearized Nernst-Planck-Poisson equation, which could lead to the oversimplification of ion dynamics in electrolytes. To better understand the polarization mechanism, it is critical to solve the fully coupled, nonlinear Nernst-Planck-Poisson equations in such pore-scale numerical simulations.

The paper is organized as follows. First, the theoretical background of diffuse layer polarization is briefly reviewed. The numerical approach used to solve the Nernst-Planck-Poisson equations is then verified by considering a

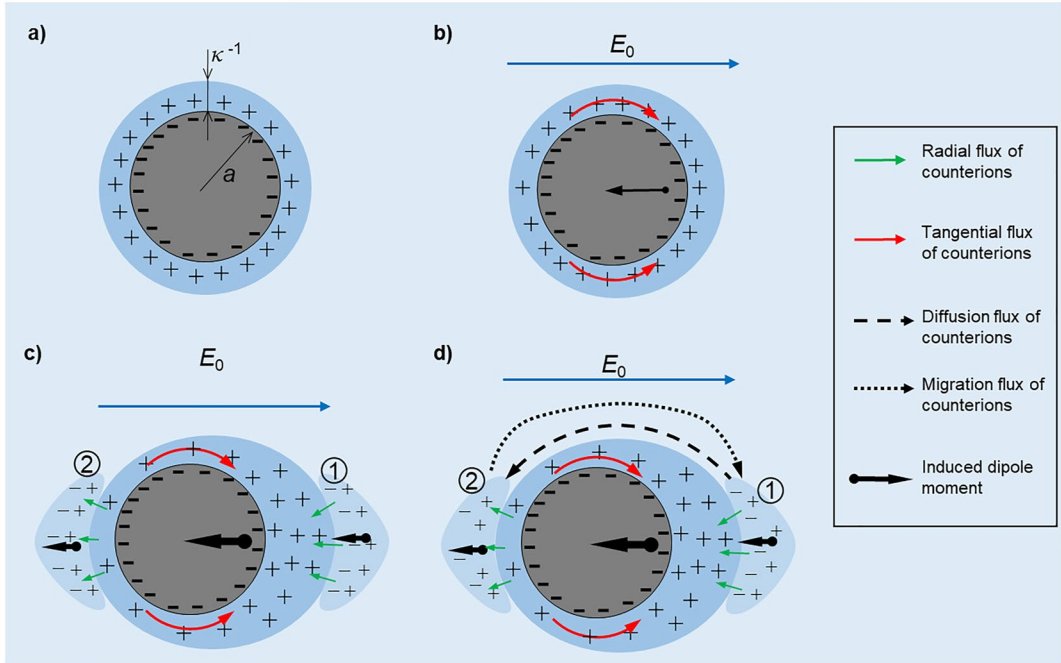

Figure 1. Conceptual model of the diffuse layer polarization around a spherical grain with a negatively charged surface (Chelidze & Gueguen, 1999): (a) counterion distribution before applying an external electric field E_0, (b) tangential movement of counterion and induced dipole moment during the polarization, (c) counterion distribution and induced dipole moment outside the diffuse layer (regions 1 and 2) after a short time interval in response to a non-equilibrium concentration of charges in the diffuse layer, and (d) diffusion and migration fluxes of counterions between regions 1 and 2 due to concentration (or salinity) difference (Bücker et al., 2019); at this stage, the electrolyte beyond the regions 1 and 2 is still neutral but their salinity has been increased (decreased) on the right (left) side of the grain. The start and end positions of the black arrow define the charge separation distance, and the thickness of the arrow shows the relative magnitude of the induced dipole moment. Tangential and normal movements of counterions are indicated by red and green arrows, respectively. Diffusion and migration fluxes of counterions are indicated by dashed and dotted lines, respectively. The grain radius is a, and the Debye length is κ^{-1}.

model with analytical solutions. Afterward, the diffuse layer polarization of a charged grain is numerically simulated, and the associated IP responses are calculated and compared to existing theoretical models. Detailed information on the local ion flux, charge separation, and induced dipole moment are provided to give insights into the pore-scale mechanism of diffuse layer polarization. Lastly, the mechanism of salinity effect on diffuse layer polarization is examined. Major conclusions are summarized at the end of this paper.

2. Theoretical Background

This section briefly reviews the concept model, governing equations, and analytical model of diffuse layer polarization around a spherical grain under an external electric field.

2.1. Conceptual Model

Diffuse layer polarization of a spherical grain in the electrolyte is an electrochemical process, which has been nicely summarized with a conceptual model in the review paper of Chelidze and Gueguen (1999). Here, we briefly review the ion dynamics within and outside the diffuse layer in response to an external electric field. Consider a negatively charged spherical grain (Figure 1). For simplicity, only the diffuse layer of the grain is shown in Figure 1, and the Stern layer is absent. The cation concentration in the diffuse layer is much higher than that in the bulk solution to shield the surface charges. Consequently, the electrical potential in the diffuse layer is also different from that in the bulk solution. For a negatively charged surface (Figure 1a), the electrical potential in the diffuse layer is negative, and its magnitude decays exponentially with distance from the surface. The thickness of the diffuse layer is usually characterized by the Debye length κ^{-1}.

After applying an external electric field E_0 (Figure 1b), both cations and anions in the diffuse layer will move (Figure 1b). First, tangential movement of counterions (and coions, not shown in Figure 1) around the grain will occur (red arrow in Figure 1b). Due to different transport numbers of cations and anions, a net ionic flux is generated, resulting in ion depletion at one side of the grain and ions enrichment on the other side of the grain. That said, the diffuse layer is deformed under the external electric field. This deformed diffuse layer (net in positive) and the surface charges (negative) then form a dipole moment, pointing from the center of the deformed diffuse layer to the center of the grain (black arrow in the grain in Figure 1b). This process has been modeled with Schwarz (1962) model.

Since the ion exchange between the diffuse layer and bulk solution is allowed (green arrow in Figure 1c), ions in the bulk solution right next to the diffuse layer will respond to the deformed diffuse layer (regions 1 and 2 in Figure 1c; Chelidze & Gueguen, 1999). For instance, at the left side of the grain, a cloud of cations and anions can be separated (region 2) due to the cation deficit on the left side of the diffuse layer. Similarly, charge separation also develops in the bulk solution at the right side of the grain (region 1 in Figure 1c). In Chelidze and Gueguen (1999), developed clouds of cation and anion separations (regions 1 and 2 in Figure 1c) are termed as diffuse clouds. The driving force for their formation is the net charge in the EDL (Figure 1b). The exchange of ions between the diffuse layer and the bulk solution happens within a short time interval and is on the order of $\sim 1/(\kappa^2 D)$ (Chelidze & Gueguen, 1999). It is noted that this short-time process was missing from the most recent IP modeling, but, as will be shown later, the numerical simulation in this study does confirm its existence. It should be noted that at this stage, the electrolyte beyond the regions 1 and 2 is still neutral but their salinity has been increased (decreased) on the right (left) side of the grain in Figure 1d.

In a longer time interval, the diffusion and migration of ions between the two diffuse clouds (regions 1 and 2 in Figure 1d) will happen and reach equilibrium. The characteristic time of this polarization is associated with the grain size and on the order of $a^2/(2D)$, and it has been addressed in many IP modeling studies (e.g., Bücker et al., 2019; Lyklema et al., 1983). These tangential, normal, diffusion and migration fluxes of ions driven by an electric field and ion concentration gradient will eventually reach equilibrium, and a full polarization is realized (Figure 1d). As shown in Figure 1d, the induced dipole moments of at full polarization are associated with two length scales: one on the order of the grain size a and one close to the Debye length κ^{-1}.

2.2. Nernst-Planck-Poisson Equations

The ionic fluxes and electrical potential within and outside the diffuse layer during polarization can be described by the Nernst-Planck-Poisson equations. The total ionic flux density $\mathbf{j}_i$ (mol m^{-2} s^{-1}) of specie i has two components: diffusion flux density $\mathbf{j}_i^d$ induced by ion concentration gradient ∇c_i (mol m^{-4}) and migration flux density $\mathbf{j}_i^{\mathrm{m}}$ due to electric field $\mathbf{E}$ (V m^{-1}) (or electrical potential gradient $\nabla\phi$). Thus, $\mathbf{j}_i$ can be written as (e.g., Schwarz, 1962)

$$\mathbf{j}_i = \mathbf{j}_i^{\mathrm{d}} + \mathbf{j}_i^{\mathrm{m}} = -D_i \nabla c_i - D_i \frac{z_i e}{k_{\mathrm{B}} T} c_i \nabla \phi \tag{1}$$

where D_i (m^2 s^{-1}) and z_i (-) are, respectively, the diffusion coefficient and charge number (positive for cations and negative for anions) of ion i, e is the elementary charge (1.6×10^{-19} C), $k_{\mathrm{B}} = 1.38 \times 10^{-23}$ m^2 kg s^{-2} K^{-1} is Boltzmann's constant, and T (K) is temperature. The above equation is known as the Nernst-Planck equation. The electrical potential ϕ (V) can be related to total charge density ρ (C m^{-3}) by the Poisson equation,

$$\nabla^2 \phi = -\frac{\rho}{\varepsilon} \tag{2}$$

in which ε (F m^{-1}) is the permittivity of the electrolyte. Equations 1 and 2 are the coupled, nonlinear Nernst-Planck-Poisson equations. It is noted that some existing studies used the linearized form of these equations to study the electrochemical polarizations (e.g., Bücker et al., 2018, 2019), but this linearization may not correctly describe the ion dynamics in the electrolyte (e.g., Bazant et al., 2004).

Considering the continuity equation, we have the divergence of ionic flux equal to the time rate change of charge density ρ_i and source rate s_i (C m^{-3} s^{-1}) of specie i, expressed as

$$\nabla \cdot \mathbf{j}_i = \frac{\partial \rho_i}{\partial t} + s_i. \tag{3}$$

Assuming no charge is created or destroyed (i.e., no chemical reaction occurs), Equation 3 becomes

$$\nabla \cdot \mathbf{j}_i = \frac{\partial \rho_i}{\partial t}. \tag{4}$$

Take the NaCl solution as an example. Equations 1 and 4 are applied to both Na^+ and Cl^-, and then the total charge density ρ is the sum of individual species, expressed as

$$\rho = \sum \rho_i = \sum F c_i z_i \tag{5}$$

where F is the Faraday constant (96,485 C mol^{-1}). Of note, c_i has the unit of mol $m^{-3,}$ and ρ_i has the unit of C m^{-3}; thus, the Faraday constant is required to link ρ_i and c_i.

2.3. Fixman Model

For a spherical grain in the electrolyte, the effective complex conductivity σ^*_{eff} (S m^{-1}) of this grain-electrolyte system can be generally treated with Wagner's theory, having the following expression (e.g., de Lima and Sharma, 1992)

$$\sigma^*_{eff} = \sigma^*_w \left[\frac{2\sigma^*_w + \overline{\sigma}^*_s - 2p\left(\sigma^*_w - \overline{\sigma}^*_s\right)}{2\sigma^*_w + \overline{\sigma}^*_s + p\left(\sigma^*_w - \overline{\sigma}^*_s\right)} \right] \tag{6}$$

where p (-) is the volumetric fraction of the grain in the system, σ^*_w (S m^{-1}) is the complex conductivity of the electrolyte, and $\overline{\sigma}^*_s$ is the apparent complex conductivity of the grain. In the absence of EDL polarization, $\overline{\sigma}^*_s$ (S m^{-1}) is simply the intrinsic complex conductivity of the grain σ^*_s. When the EDL is polarized, an additional term $\Delta\sigma^*_s$ (S m^{-1}) is incorporated into σ^*_s to account for the effect of EDL polarization. Thus, the grain has an apparent complex conductivity $\overline{\sigma}^*_s = \sigma^*_s + \Delta\sigma^*_s$.

Assuming a thin diffuse layer, Fixman (1980) solved the Nernst-Planck-Poisson equations for a spherical grain with a surface charge density Q_s (C m^{-2}) under an oscillating external electric field with angular frequency ω (rad s^{-1}). In Fixman's solution, $\overline{\sigma}^*_s$ is embedded in the dipolar coefficient γ_p (-), which can be expressed as

$$\gamma_p = \frac{\overline{\sigma}^*_s - \sigma^*_w}{\overline{\sigma}^*_s + 2\sigma^*_w} = -\frac{1 - \delta(1+Y)}{2 + \delta(1-2Y)} \tag{7}$$

where $\delta = Q_s/(ac_0)$, c_0 (mol m^{-3}) being the ion concentration of the electrolyte and a (m) being the grain radius. The term Y in Equation 7 is expressed as

$$Y = -[f(\lambda a) - Hf(-\lambda a)]/[g(\lambda a) - Hg(-\lambda a)] \tag{8}$$

where the functions $f(x)$, $g(x)$, and H are respectively expressed as

$$f(x) = (1+x)e^{-x}, \tag{9}$$

$$g(x) = \left(2 + 2x + x^2\right)e^{-x}, \tag{10}$$

and

$$H = g(\lambda R)/g(-\lambda R). \tag{11}$$

In the above equations, $\lambda = (1+j)\sqrt{\omega/(2D)}$ (D being the diffusion coefficient of counterions in the diffuse layer and j being the imaginary number) and R (m) refers to the distance from the grain center to the point where the electrical potential reduces to zero under unperturbed conditions. Note that de Lima and Sharma (1992) give a simplified expression for Y (see their Equation 8) by assuming an infinitely large R value. However, as will be shown later, the parameter R has a significant influence on both the shape and magnitude of $\overline{\sigma}^*_s$; in general, it should not be taken as an infinitely large value.

3. Validation of Numerical Approach

In this study, the Nernst-Planck-Poisson equations are numerically solved using the finite element method software Comsol Multiphysics (ver. 5.6, COMSOL, Inc., MA, USA). To validate the numerical approach, we

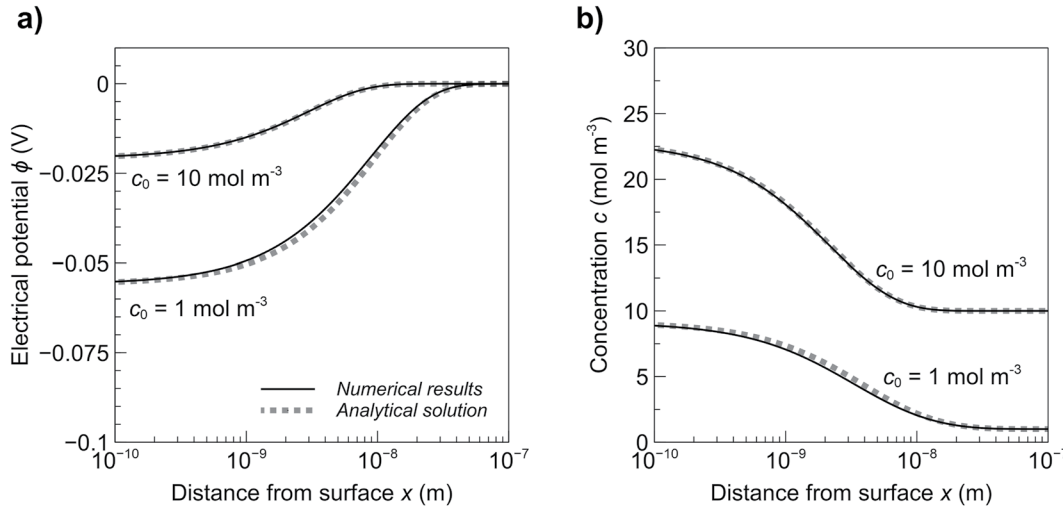

Figure 2. Distribution of electrical potential ϕ and Na^+ concentration c near a charged plate at the static condition: (a) ϕ and (b) c. Numerical solutions are from Comsol, and analytical solutions are calculated from the Gouy-Chapman theory (Equations 12 and 13). Two ion concentrations c_0 are considered for the NaCl solution.

consider a parallel plate capacitor filled with NaCl solution (Figure S1 in Supporting Information S1). For this 1D model, the analytical solutions to the Poisson-Nernst-Planck equations are available under both static conditions (e.g., Gouy-Chapman theory) and dynamic conditions (e.g., Hashemi Amrei et al., 2020). The two plates have a distance of 2 μm and are negatively charged with a surface charge density $Q_s = -0.005$ C m^{-2}. The diffusion coefficient D is 1.3×10^{-9} for Na^+ and 2.0×10^{-9} m^2 s^{-1} for Cl^{-1} in both diffuse layer and bulk solution. The temperature is set as 20°C.

Under static conditions, the charged plates attract Na^+ to form the diffuse layer, within which both the ion concentration c and electric potential ϕ deviate from those in the bulk solution. The Tertiary Current Distribution module of Comsol is used to calculate ϕ and c near the plate surface with two c_0 values (1 and 10 mol m^{-3}), and the numerical results are shown in Figure 2. Analytical solutions of ϕ and c of cations from Gouy-Chapman theory (e.g., Eliaz & Gileadi, 2019) are expressed as

$$\phi(x) = \frac{2N_A k_B T}{F} \operatorname{asinh}\left(\frac{-\rho_0}{\sqrt{8\varepsilon c_0 N_A k_B T}}\right) \exp\left(-\frac{x}{\kappa^{-1}}\right) \tag{12}$$

and

$$c(x) = c_0 \exp\left(\frac{-\phi(x)F}{N_A k_B T}\right) \tag{13}$$

where x (m) is the distance from the surface, N_A (mol^{-1}) is Avogadro's constant, and κ^{-1} (m) is the Debye length. The analytical solutions from Equations 12 and 13 are also plotted in Figure 2 for comparison. As shown in the figures, numerical results from Comsol are nearly identical to the analytical solutions for both c_0, proving the accuracy of the solver in Comsol for Nernst-Planck-Poisson equations at static conditions.

To simulate dynamic conditions, a sinusoidal electric field E_0 with frequency f is applied to the parallel plate (Figure S1 in Supporting Information S1). The applied electrical potentials at the two plates have opposite signs, and each varies from −10 to 10 mV; thus, the maximum voltage difference is 20 mV across the plates. Under this electric field, ions in the diffuse layer and bulk solution will migrate, inducing ion concentration gradient, which in turn will drive diffusive ionic fluxes and affect the electrical potential. This dynamic, coupled process is simulated by solving Nernst-Planck-Poisson equations with Comsol's Frequency Domain Perturbation solver. In the simulation, c_0 is set as 1 mol m^{-3}, and other properties are kept unchanged. The initial c and ϕ distributions near the plate surface use static solutions (e.g., Figure 1). The calculated perturbations in ϕ and c due to E_0 are shown in Figure 3 for $f = 10^2$ and 10^6 Hz. The analytical solutions from Hashemi Amrei et al. (2020) are also plotted

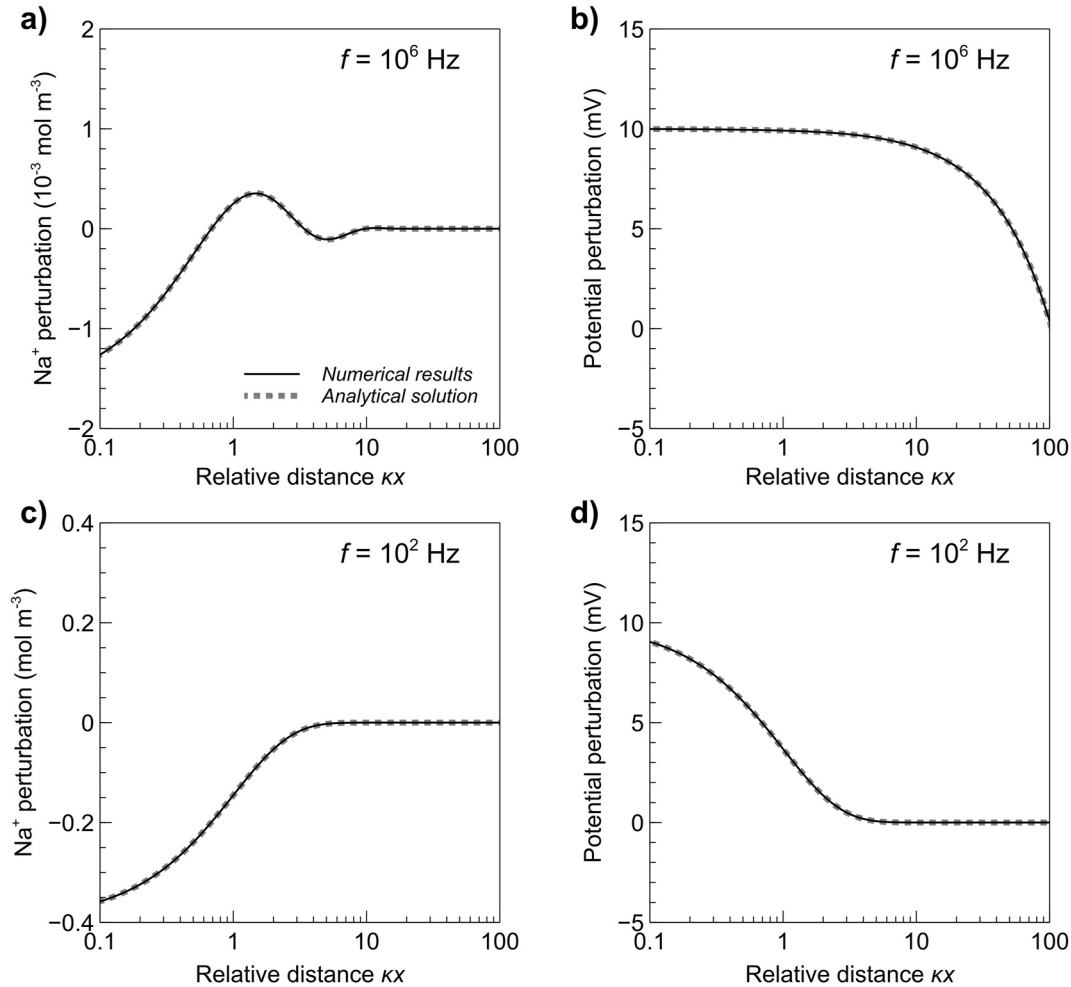

Figure 3. Perturbations in Na^+ concentration and electrical potential near one plate under an oscillating electric field E_0 with frequency f: (a) Na^+ concentration perturbation at $f = 10^6$ Hz, (b) electric potential perturbation at $f = 10^6$ Hz, (c) concentration perturbation at $f = 10^2$ Hz, and (d) electric potential perturbation at $f = 10^2$ Hz. The distance x from the plate surface is normalized by Debye length κ^{-1}. Analytical results are calculated using the perturbation solution in Hashemi Amrei et al. (2020).

in Figure 3 for comparison. In Comsol, a Harmonic Perturbation subnode can be assigned to the two plates to apply the voltage amplitude perturbation. Since the perturbation analysis is conducted in the frequency domain, only the maximum voltage is needed to define the applied perturbation. Similarly, the output from the Frequency Domain Perturbation solver only gives the magnitude of the perturbation in concentration/potential at a given frequency. Thus, in this study, all the reported perturbations in ion concentration and electrical potential are the maximum perturbed values, and no phase information is provided.

For $f = 10^6$ Hz, ions near the plate surface do not have enough time to respond to the external field, and thus the Na^+ perturbation is very small (Figure 3a). In contrast, Na^+ has adequate time to react to E_0 at $f = 100$ Hz, and the associated Na^+ perturbation is significant (Figure 3c), about an order higher than that at $f = 10^6$ Hz. The perturbed ϕ are also quite different for these two frequencies (Figures 3b and 3d). At $f = 10^6$ Hz, the changes in potential perturbation occur mainly in the bulk solution (e.g., $\kappa x > 10$ in Figure 3b). Conversely, at $f = 10^2$ Hz, most of the changes in potential perturbation are within the diffuse layer (e.g., $\kappa x < 1$ in Figure 3d). These distinct responses at high and low frequencies are well captured by the numerical solution, and the numerical results agree perfectly with the analytical solutions, as shown in Figure 3. These agreements indicate that the Frequency Domain Perturbation solver of Comsol can accurately solve the fully-coupled, nonlinear Nernst-Planck-Poisson equations under dynamic conditions. The linearized Nernst-Planck-Poisson equations are also solved using Comsol (Bücker et al., 2019) for this parallel plate model. The simulated ion concentration and potential deviate

significantly from the analytical solution, and much information on ion dynamics near the plate is missing, especially at low frequencies (Figure S2 in Supporting Information S1).

4. Revisiting Diffuse Layer Polarization

In this section, we revisit the mechanism of diffuse layer polarization by analyzing the macroscopic and microscopic responses of the grain-electrolyte system calculated from numerical simulations.

4.1. Numerical Model

We consider a non-conducting spherical grain immersed in NaCl electrolyte with $c_0 = 1$ mol m^{-3}. The grain is negatively charged on the surface with $Q_s = -0.02$ C m^{-2} and has a radius a of 10 μm. In the simulation, a cylindrical domain with a height of $10a$ and a radius of $5a$ is considered, and the grain is put at the center of the domain (Figure S3 in Supporting Information S1). This geometric setup gives a grain volume fraction $p = 0.5\%$, indicating a dilute condition. In the simulation, the diffusion coefficient D is set as 1.3×10^{-9} m^2 s^{-1} for both Na^+ and Cl^-; a sinusoidal electrical field E_0 with magnitude 10^{-8} V/m is applied along the axis of the cylinder. The numerical model is axially symmetric, and thus, the simulation can be set as a 2D axial symmetry problem to reduce computational costs. The boundary of the cylinder has a constant ion concentration of c_0 so that no charge will accumulate at the model boundary.

The ion concentrations c (Na^+ and Cl^-) and electrical potential ϕ of the grain-electrolyte system are calculated by solving the Nernst-Planck-Poisson equations with Comsol. The external electric field with different frequencies f is applied. For each f, the electrical potential at both top and bottom of the cylinder (ϕ_{top} [V] and ϕ_{bottom} [V]) are determined; total current I (A) passing through the model (along the cylindrical axis) is determined as a sum of the conduction and displacement currents. By considering the geometry of the domain, the effective complex conductivity σ^*_{eff} of the grain-electrolyte system can then be calculated as

$$\sigma^*_{eff} = \frac{L}{A}\frac{I}{\phi_{top} - \phi_{bottom}} \tag{14}$$

where L (m) and A (m^2) are the length (height) and cross-section area of the cylinder, respectively.

4.2. Macroscopic IP Responses

In the geophysical community, the IP responses are commonly quantified with two different but related parameters: (a) imaginary conductivity $\sigma''_{eff} = \text{imag}(\sigma^*_{eff})$ and (b) permittivity $\varepsilon_{eff} = \sigma''_{eff}/\omega$. The calculated σ''_{eff} and ε_{eff} of the grain-electrolyte system are shown in Figure 4 for frequencies ranging from 10^{-2} and 10^7 Hz. In the calculation, we have two treatments regarding the value of σ^*_w. In Figures 4a and 4b, σ^*_w is equal to $\sigma_w + j\omega\varepsilon_w$ where ε_w is the permittivity of water contributed by the dipolar polarization of water molecules. Although this treatment gives a result consistent with experimental measurements (e.g., Leroy et al., 2008), the presence of dipolar polarization of water in Figures 4a and 4b will mask the diffuse layer polarization at intermediate frequencies (around 10 Hz). To better visualize the effect of diffuse layer polarization, the effect of dipolar polarization of water is removed and the results are shown in Figures 4c and 4d. For numerical simulation results, removing the influence of water dipolar polarization is realized by excluding the displacement current in calculating the total current density; for theoretical modeling, this is done by assigning $\sigma^*_w = \sigma_w$ in Equation 6.

The IP responses in Figure 4a (σ''_{eff}) and Figure 4b (ε_{eff}) are typical to saturated granular materials (e.g., Leroy et al., 2008). At high frequencies (>10^3 Hz), the $\sigma''_{eff} - f$ curve is a straight line in a log-log plot (Figure 4a), indicating that diffuse layer polarization has yet contributed to σ''_{eff} and ε_{eff}. Actually, during this frequency range (>10^3 Hz), it is the dipolar polarization of water that contributes to the calculated σ''_{eff} and ε_{eff}. This can be seen in Figure 4b as a constant ε_{eff} that is close to water permittivity $80\varepsilon_0$ (ε_0 being the vacuum permittivity). As the frequency decreases, the polarization of the diffuse layer starts to contribute to the IP responses of the grain-electrolyte system. It manifests itself as an increased ε_{eff} around 10 Hz in Figures 4b and 4a shift of the $\sigma''_{eff} - f$ curve toward the lower frequency direction in Figure 4a. As the frequency further decreases (<10^{-1} Hz), the diffuse layer has been fully polarized; the effective permittivity of the grain-electrolyte system becomes a constant (Figure 4b), and the $\sigma''_{eff} - f$ curve becomes a straight line again (Figure 4a). The presence of the diffuse layer polarization gives a permittivity increment of $\sim 2{,}500\varepsilon_0$ in the frequency range between 10^{-1} and 10^3 Hz.

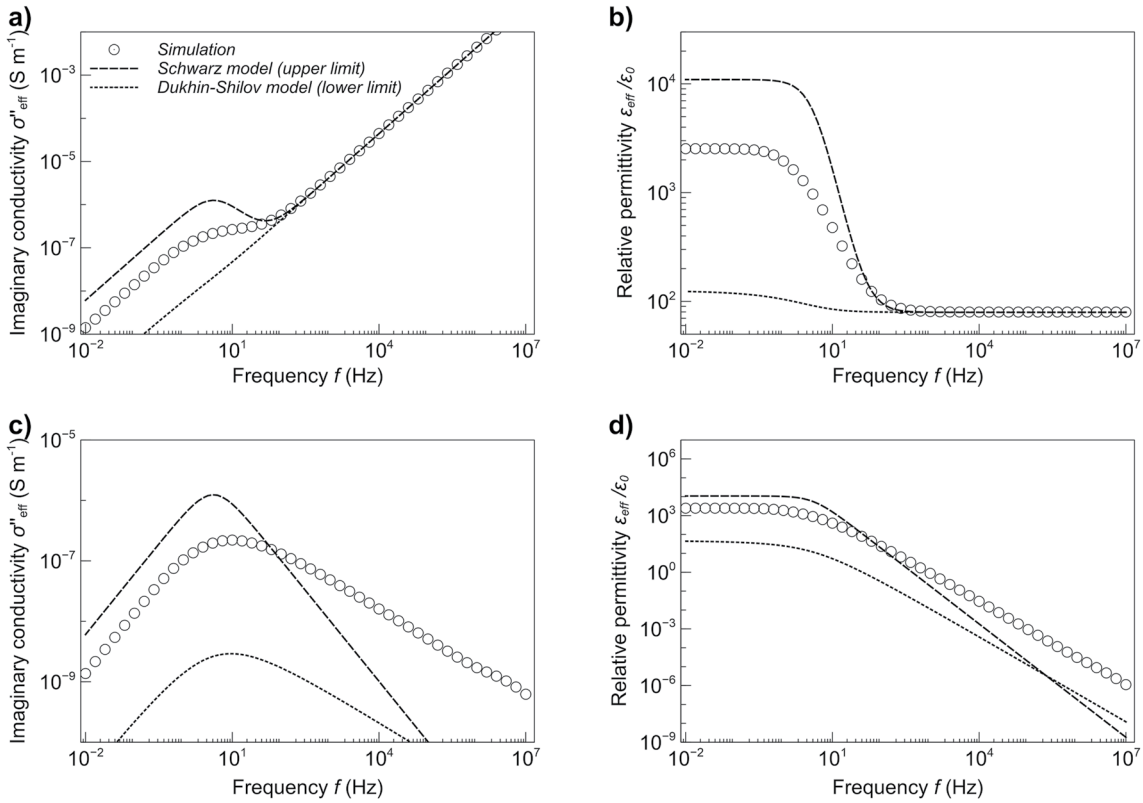

Figure 4. Induced polarization (IP) of a spherical grain (radius $a = 10^{-6}$ m) in NaCl solution (ion concentration $c_0 = 1$ mol m^{-3}). (a) and (c) Are the effective imaginary conductivity σ''_{eff}; and (b) and (d) are the effective permittivity ε_{eff} results, which are normalized by the vacuum permittivity ε_0. For (a) and (b), the IP responses contain both the dipolar polarization of water and diffuse layer polarization. For (c) and (d), the effect of dipolar polarization of water is excluded for better visualization of the diffuse layer polarization. The upper and lower limits refer to Schwarz (1962) model and the Dukhin-Shilov model (Shilov et al., 2001), respectively.

In Figures 4c and 4d, since the dielectric properties of water are removed, the responses of σ''_{eff} and ε_{eff} are only from the diffuse layer polarization. Figure 4c shows an important feature that was not revealed in Figure 4a. That is, σ''_{eff} induced by diffuse layer polarization is not symmetric with respect to f in a log-log plot. This asymmetric σ''_{eff} response may not be described by the classic Cole-Cole model, which has been commonly used for various geological materials (e.g., Chen et al., 2008; Jougnot et al., 2010; Nordsiek & Weller, 2008). Additionally, it is easy to identify the characteristic frequency f_c of diffuse layer polarization in Figures 4c and 4d. Of note, f_c is defined as the frequency at which σ''_{eff} reaches a maximum. For this grain-electrolyte system, f_c is determined as ~10 Hz.

4.3. Tangential Versus Normal Ionic Fluxes

Numerical solutions of Nernst-Planck-Poisson equations produce rich information on the ion dynamics within and near the diffuse layer. We use this microscopic information to analyze the relative importance of tangential (or circumferentially) and normal (or radial) ionic fluxes in diffuse layer polarization. To guide the analysis, we also plotted two limiting theories in Figure 4: the Schwarz model (Schwarz, 1962) and Dukhin-Shilov model. Due to length constraints, the mathematic equations of the two theories are not repeated here. Readers are referred to the original papers (Schwarz, 1962) or some recent studies (e.g., Bücker et al., 2019; Leroy et al., 2008). Here, we only summarize the general assumptions and related physical implications of the two limiting theories. While the Schwarz model assumes the ions in the EDL only move tangentially, the Dukhin-Shilov theory ignores the tangential movement of ions and only considers the normal ionic flux (see discussions in Fixman, 1980). The tangential movement of ions in the EDL generally induces a larger dipole moment than normal ionic movement. This is because tangential movement of ions is usually within the EDL, and thus more counterions are involved in the polarization than coions; in contrast, the normal movement of ions could be away from the

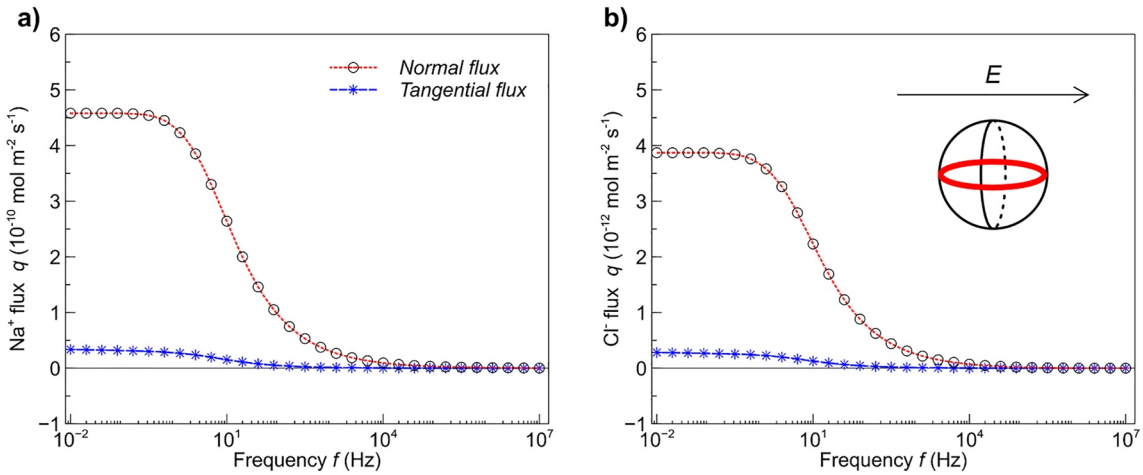

Figure 5. Tangential and normal fluxes q of ions in the diffuse layer during polarization: (a) Na^+ and (b) Cl^-. "Tangential" and "normal" indicate the flux direction is tangential and normal to the grain surface, respectively. Note that the y-axis scales in (a) and (b) are different. All the flux data are positive in the above figures; the y-axis extends into negative for better visualization of the data points close to zero. The positions of flux data used in the calculation are highlighted in red in (b).

grain surface, thus involving a similar amount of counterions and coions. Considering a fixed charge separation distance, tangential movement is then associated with more net charges, which will give a higher polarizability (and thus enhanced permittivity) than that of the normal movement. Therefore, the Schwarz and Dukhin-Shilov models can be regarded as the upper and lower limits of the EDL polarization, respectively.

While using the Schwarz and Dukhin-Shilov models, the characteristic relaxation time $\tau_c = 1/(2\pi f_c)$ is calculated as $a^2/(2D)$ (Schwarz, 1962). Using the parameters a and D, we calculate $\tau_c = 0.038$ s, which corresponds to a characteristic frequency of 4 Hz, close but lower than the value observed from simulated results (~10 Hz; Figure 4c). Regarding the enhanced permittivity (Figure 4b), the simulated values are well-bounded by the upper and lower limits. While the pure tangential movement of ions in EDL (Schwarz model) gives a permittivity enhancement of $\sim 10^4 \varepsilon_0$, pure normal ionic movement (Dukhin-Shilov model) only gives $\sim 40\varepsilon_0$. This highlights the importance of the tangential movement of ions in EDL polarization. It is also noted that the Schwartz model and Dukhin-Shilov model can only be regarded as the limits at low frequencies at which the EDL has been fully polarized. At higher frequencies, the Schwarz model may give a smaller enhanced permittivity (e.g., at 10^4 Hz in Figures 4c and 4d) because it is much more difficult to mobilize a tangential ionic movement than a normal movement with an external electric field. The relative easiness of normal flux over tangential flux is reflected in Figure 4c as the Dukhin-Shilov model having a broader σ''_{eff} distribution than the Schwarz model.

The simulated IP responses are bounded by the upper and lower limits, implying that diffuse layer polarization involves both tangential and normal movements of ions. To demonstrate this, we use Na^+ and Cl^- movements in the inner region of the diffuse layer (i.e., right next to the grain surface) as an example. For simplicity, only the data on the great circle parallel to the external electric field are used (highlighted as red in Figure 5b). The (arithmetic) average fluxes q of Na^+ and Cl^- in both tangential and normal directions are calculated, and the results are plotted in Figure 5 for different frequencies. It is shown that both Na^+ and Cl^- move under the external electric field. Generally, the magnitude of Cl^- flux (Figure 5b) is about 2 orders smaller than Na^+ fluxes (Figure 5a), indicating the diffuse layer polarization is dominantly contributed by counterions (Na^+) fluxes. In Figure 5a, both normal and tangential ionic fluxes of Na^+ are significant, implying that fluxes in both directions contribute to polarization. Compared to tangential flux, the normal movement of ions, however, is much larger. For example, Na^+ flux in the tangential direction at 0.01 Hz (blue line in Figure 5a) is about 10 times smaller than that in the normal direction (red line in Figure 5a). Despite the small ionic flux in the tangential direction (Figure 5a) during diffuse layer polarization, its contribution to the permittivity enhancement is however dominant over normal flux (see Figures 4c and 4d).

4.4. Polarization Outside of the Diffuse Layer

In addition to ions within the EDL, as shown in Figure 1, ions in the bulk solution may also polarize during the diffuse layer polarization by forming zones right next to EDL with charge accumulation and concentration

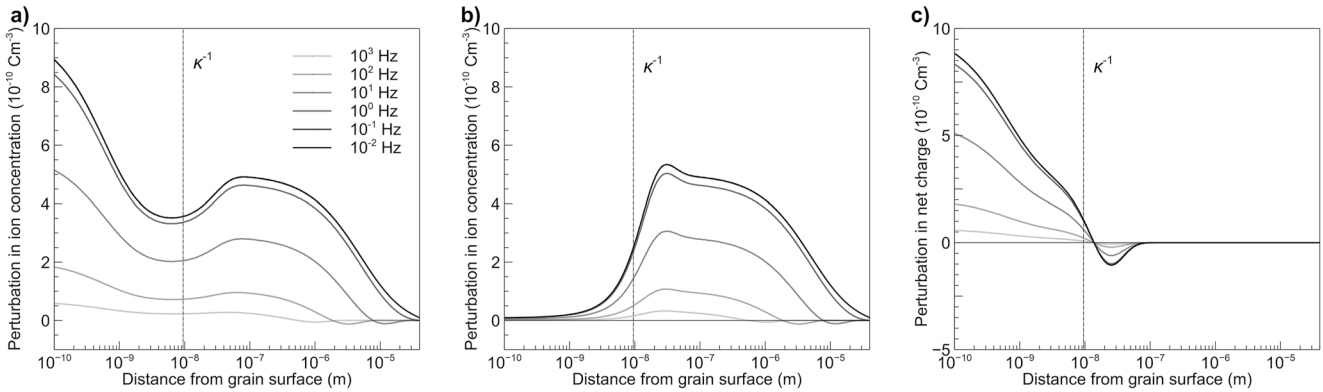

Figure 6. Perturbations in ion concentrations within the diffuse layer and in the bulk solution along the axis of symmetry of the grain-electrolyte system at different frequencies: (a) Na^+, (b) Cl^-, and (c) net charge. Debye length κ^{-1} in the figure is calculated using the Gouy-Chapman theory.

gradients. Here we analyze the relative importance of this concentration gradient using the concentration data from numerical simulations. For demonstration purposes, only the data along the axis of symmetry are used in the analysis. The spatial distribution of perturbed ion concentration (Δc_i) is shown in Figure 6 for different frequencies. In the figure, the position of the Debye length $\kappa^{-1} = 9.5 \times 10^{-9}$ m is also indicated to facilitate the discussion.

As shown in Figure 6, the external field-induced Δc_i are predominantly counterions (Na^+) within the diffuse layer (i.e., distance smaller than the Debye length κ^{-1}). For instance, at $f = 10^{-2}$ Hz, the Na^+ perturbation in the diffuse layer is roughly from 4×10^{-10} to 8×10^{-10} C m^{-3} (Figure 6a); in contrast, the Cl^- perturbation is generally smaller than 2×10^{-10} C m^{-3} (Figure 6b). Due to this perturbation, the center of Na^+ in the diffuse layer does not have the same location as the surface charges (Figure 1c). This induced charge separation creates a dipole moment (Figure 1c) and contributes to enhanced permittivity. Perturbations in Na^+ and Cl^- concentrations also occurred in the bulk solution, for example, in regions from 10^{-8} to 10^{-5} m, as shown in Figure 6. It appears that perturbations in the bulk solution are comparable to those in the diffuse layer. If we consider the net charge (Figure 6c), the concentration in the bulk solution is, however, very small, about one order lower than the net charge concentration in the diffuse layer.

To compare Δc_i within ($x < \kappa^{-1}$) and outside EDL ($x > \kappa^{-1}$), we calculated two parameters for the perturbed ions around the grain surface (same as Figure 5) and along the axis of symmetry of the grain-electrolyte system (same as Figure 6): (a) the separation distance between the centers of perturbed Na^+ and Cl^- and (b) the magnitude of induced dipole moment. For polarization within the diffuse layer, the perturbed ion along the great circle of the grain parallel to the external electric field (same as Figure 5) is used; the charge separation is from the center of negative surface charge (i.e., grain center) to the center of perturbed Na^+ (see Figure 1c). For ion clouds outside the diffuse layer, the perturbed ion along the axis of symmetry of the grain-electrolyte (same as Figure 6) is used; the charge separation is the distance between the centers of the perturbed Na^+ and Cl^- in diffuse clouds. In the calculation, the distance x_i^c of Na^+ (or Cl^-) center to the grain surface is defined as the position that divides the total perturbed ions in this region into two equal halves. It can be calculated using the following equation

$$\int_{x_{\min}}^{x_i^c} \Delta c_{idx} = \frac{1}{2} \int_{x_{\min}}^{x_{\max}} \Delta c_{idx} \tag{15}$$

where $x_{\min}$ and $x_{\max}$ are the minimum and maximum distances from the grain surface considered in the calculation. The calculated charge separation distances are shown in Figure 7a for frequencies from 10^{-2} to 10^{7} Hz. The dipole moment is calculated as the product of charge separation distance and total (perturbed) charge quantity. Here, the total amount of charges q_i^t (mol m^{-2}) is calculated as the line integration of Δc_i (mol m^{-3}), that is, $q_i^t = \int_{x_{\min}}^{x_{\max}} \Delta c_{idx}$, and thus the unit of dipole moment in Figure 7b is in mol m^{-1}.

In Figure 7a, it is shown that the surface charge (negative) and counterions (Na^+) have a constant separation distance, $\sim 4 \times 10^{-6}$ m, which is slightly smaller than the grain radius 10×10^{-6} m. In contrast, the charge separation between Na^+ and Cl^- in the bulk solution right next to the diffuse layer is rather small, generally less than 10^{-8} m. This indicates the length scale of the concentration gradient formed outside the diffuse layer is close to

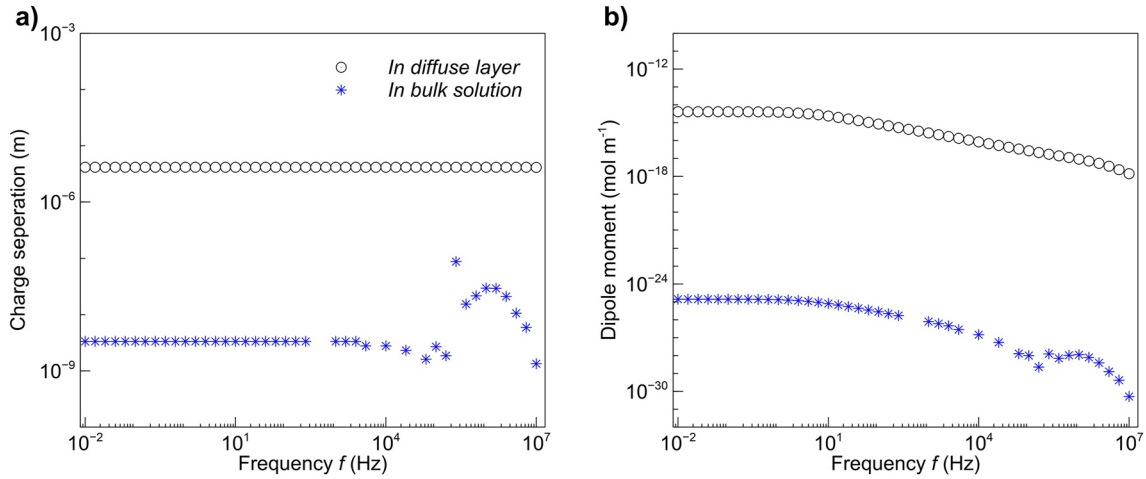

Figure 7. Perturbed ions in the diffuse layer around the grain and in the bulk solution right next to the diffuse layer: (a) charge separation distance and (b) induced dipole moment.

the Debye length $\kappa^{-1} = 9.5 \times 10^{-9}$ m (Chelidze & Gueguen, 1999). Figure 7b presents the dipole moment related to these two different ion concentration gradients (i.e., within the diffuse layer around the grain and in bulk solution right next to the diffuse layer). The dipole moment related to the former (i.e., deformed diffuse layer) is relatively large and varies mainly around 10^1 Hz, consistent with the macroscopic responses in Figures 4c and 4d. The dipole moment related to the latter (star in Figure 7b) is small but not zero, implying the concentration gradient developed in the bulk solution also contributes to polarization. However, the dipole moment formed in the bulk solution is several orders lower than that formed in the diffuse layer, and thus, its contribution to the IP responses of the grain-electrolyte system is negligible. Note that there are some spikes in the calculated charge separation at high frequencies in Figure 7a. This variation is probably due to the small domain where the calculation was performed (i.e., the axis of symmetry of the grain-electrolyte system). The actual diffuse clouds occupy a much larger region (Figure 1d). Therefore, the charge separation/dipole moment calculation based on this selected domain here may have some noise.

5. Modification to the Fixman Model

As mentioned in Section 2.3, the Fixman model incorporates both tangential and radial movements of ions in describing diffuse layer polarization. In this section, we compare the Fixman model to the simulation results to evaluate its performance. Note that the mostly-used Fixman model (e.g., in Lesmes & Morgan, 2001) was only a simplified version introduced by de Lima and Sharma (1992) by assuming the parameter R in Equation 11 as infinitely large. This simplification was suggested because R was defined as the distance from the grain center to the position where ϕ decays to zero (Fixman, 1980). We use $R = +\infty$ to calculate the theoretical results of the Fixman model, and the results are shown in Figure 8 (dotted lines). It is clear that the theoretical results underestimate the macroscopic IP responses considerably. For instance, the permittivity enhancement at 10^{-2} Hz from the theory is only $\sim 100\varepsilon_0$, much smaller than the simulated value $\sim 2{,}000\varepsilon_0$ (Figure 8b). Interesting to note that the shapes of σ''_{eff} and ε_{eff} curves from the theory resemble the numerical results quite well.

Note that ϕ decays exponentially, and it could become negligibly small at a finite distance away from the grain surface. This implies that R does not need to be assigned as $+\infty$, and a much smaller value should be sufficient. We estimate this finite distance from the spatial distribution of ion concentration perturbations shown in Figure 6. If we ignore the perturbed c_i in the bulk solution, R can be easily estimated by extrapolating the perturbed c_i in the diffuse layer into the bulk solution. Following this procedure, we estimate $R = a + 10\kappa^{-1}$ from Figure 6a. The Fixman model is used again with this new R value to calculate σ''_{eff} and ε_{eff} (dash lines in Figure 8). Interestingly, the modeled IP responses agree well with the simulated results at low frequencies (e.g., <1 Hz in Figure 8). Important to note that the grain-electrolyte system is fully polarized when f is smaller than 1 Hz. This means that the Fixman model with $R = a + 10\kappa^{-1}$ gives a correct estimation of the maximum polarization intensity. It is also noticed that theoretical σ''_{eff} and ε_{eff} deviate significantly from the simulation at high frequencies (>10 Hz),

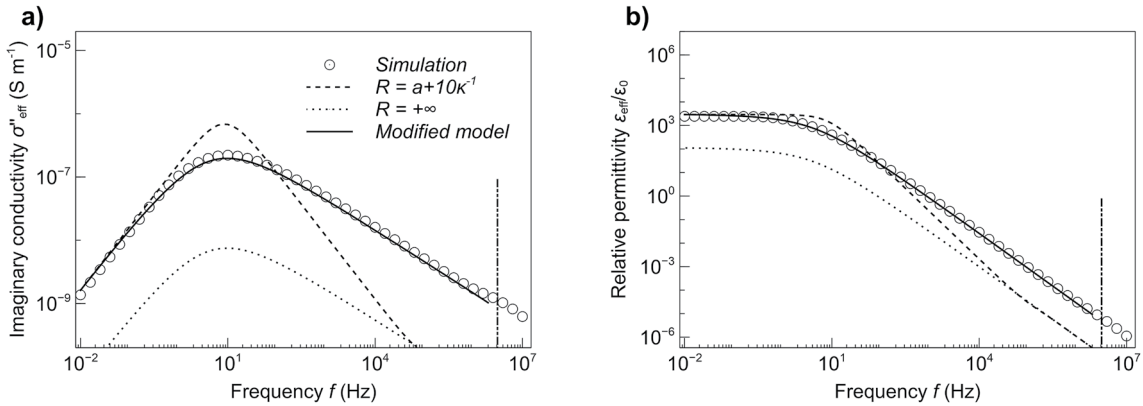

Figure 8. Comparison of simulated and modeled induced polarization (IP) responses of the grain-electrolyte system: (a) effective imaginary conductivity and (b) effective permittivity. Modeled IP responses (dash and dotted lines) were calculated using the Fixman model with two R values. The results from the modified Fixman model are also included (solid line). The vertical lines indicate the location of the characteristic frequency calculated using the Debye length as $D/(3\kappa^{-1})^2$ as described in the main text.

meaning that the polarization process (i.e., from the initiation of charge separation to a full polarization) was not correctly modeled with $R = a + 10\kappa^{-1}$.

The influence of R on modeled IP responses shown in Figure 8 implies that R plays two different roles in the Fixman model. First, R defines the region where the normal movement of ions occurs during diffuse layer polarization. A large R (e.g., $+\infty$) ensures a free exchange of ions between the bulk solution and diffuse layer; consequently, a large R will give the correct shape of macroscopic IP responses (dotted lines in Figure 8). In this regard, it is preferred to have a large R in order to better represent the dynamic polarization process. Second, R also defines the region where the complex surface conductance Σ_s^* induced by diffuse layer polarization is averaged (or upscaled) to determine $\Delta\sigma_s^*$. For a spherical region with radius Π, this upscaling process is expressed as $\Delta\sigma_s^* = 2\Sigma_s^*/\Pi$ (Niu, Prasad, et al., 2016). In order to correctly model the polarization magnitude, this upscaling process has to be properly treated; consequently, an R value that is close to the grain radius a but also includes the diffuse clouds is preferred. According to Figure 6c, $R = a + 10\kappa^{-1}$ is selected here.

To reconcile the competing requirements of R values, we suggest using $R = +\infty$ and $a + 10\kappa^{-1}$ to respectively determine the shape of $\varepsilon_{\text{eff}} - f$ (or $\sigma''_{\text{eff}} - f$) curve and the magnitude of IP (i.e., ε_{eff} at low frequency). This modification to the Fixman model (detailed equations are provided in Appendix A) is used to calculate σ''_{eff} and ε_{eff} of the grain-electrolyte system, and the results are shown in Figure 8 as solid lines. As shown, the modified model takes advantage of both a large R and an R close to a, and excellent matches are observed for both the shape and magnitude of the IP responses induced by diffuse layer polarization. In the following section, we will also test the applicability of the modified model over a large salinity range.

In Figure 8, some discrepancies are observed between the modified Fixman model and the simulation, implying the existence of an additional polarization with a characteristic frequency of around 2.5 MHz. This polarization at high frequency (~MHz) is clearly not captured by Schwarz, Dukhin-Shilov, and Modified Fixman models. It is postulated that this polarization at high frequency is related to the dipole moment formed in the diffuse clouds right next to the grain (regions 1 and 2 in Figure 1d). As mentioned, the length scale of this short-time polarization is related to the Debye length ($\kappa^{-1} = 9.5 \times 10^{-9}$ m). From Figure 6c, the charge separation (or length scale) is about $3\kappa^{-1}$. Considering $D = 1.3 \times 10^{-9}$ m^2 s^{-1}, we can calculate the time constant τ is 3.2×10^{-7} s, which corresponds to a frequency of 3.1×10^6 Hz, which is consistent with the location of the observed high-frequency polarization (Figure 8a). This relaxation time has been called "Debye time" or "time scale of charge relaxation" in some studies (e.g., Bücker et al., 2018). Therefore, it is argued here that the polarization outside the diffuse layer is related to a small length scale, about several Debye lengths.

6. Mechanism and Modeling of Salinity Effect

Numerical simulations have also been conducted for the grain-electrolyte system with different fluid salinities. The simulation results will be used (a) to evaluate if the modified Fixman model works over a broader salinity

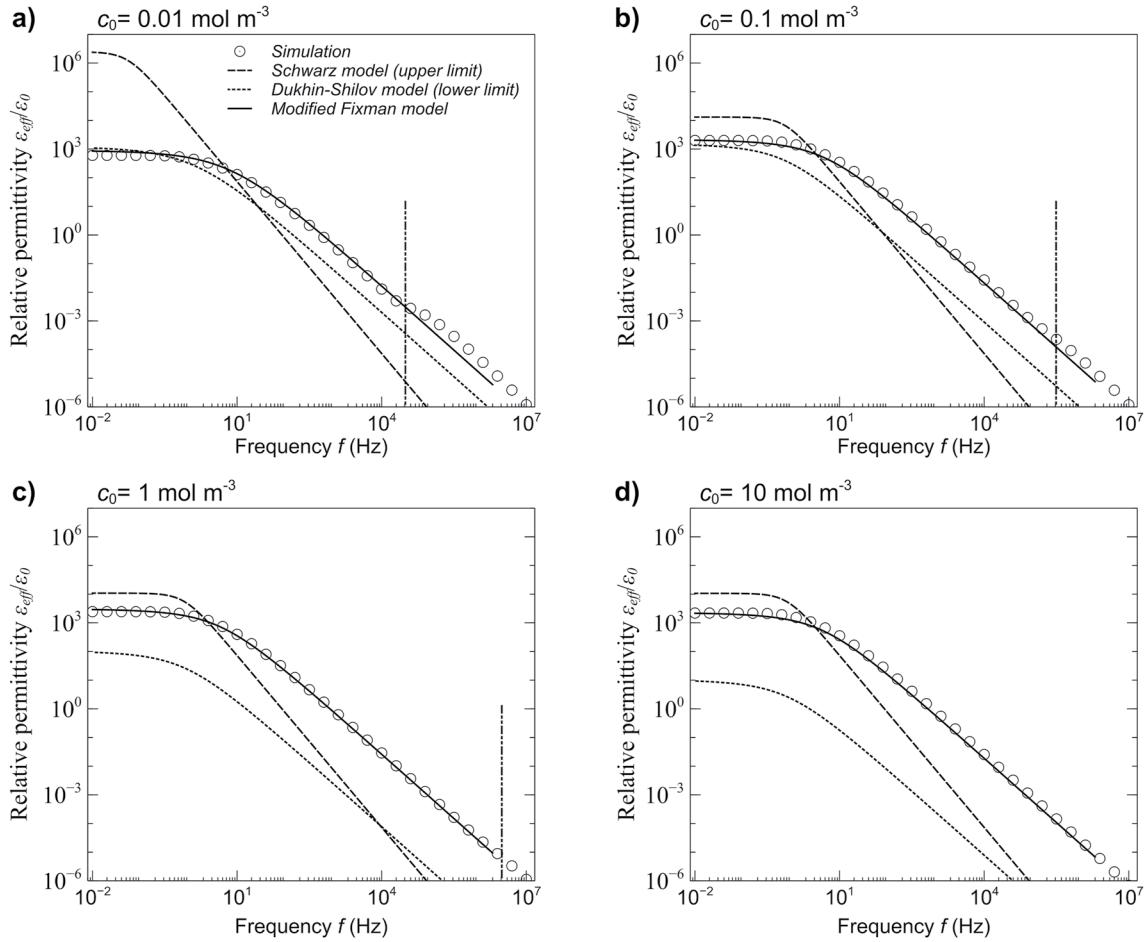

Figure 9. Simulated and modeled induced polarization responses of the grain-electrolyte system with different fluid salinity c_0: (a) $c_0 = 0.01$ mol m^{-3}, (b) $c_0 = 0.1$ mol m^{-3}, (c) $c_0 = 1$ mol m^{-3}, and (d) $c_0 = 10$ mol m^{-3}. The modeled results are from the modified Fixman model (solid line), Schwartz model (dash line), and Dukhin-Shilov model (dotted line). The vertical lines indicate the location of the characteristic frequency calculated using the Debye length as $D/(3\kappa^{-1})^2$ as described in the main text.

range and (b) to analyze, from a microscopic point of view, how the diffuse layer polarization is affected by the fluid salinity.

6.1. Modeling With the Modified Fixman Model

In total, nine salinities of the NaCl solution are considered in the numerical simulation. The range of ion concentration c_0 is between 0.01 and 100 mol m^3, and the associated fluid conductivity σ_w range is between 10^{-4} and 1 S m^{-1}, a typical range for groundwater in practice. Other parameters of the system are unchanged. Figure 9 summarizes the simulation results for four salinities (c_0 = 0.01, 0.1, 1, and 10 mol m^3). To better visualize the diffuse layer polarization, the dipolar polarization of water is not considered. The results of the modified Fixman model are also plotted in Figure 9 for comparison. The original Fixman theory (Equations 6–11) with a single R value was also applied, but it failed to fit the simulated results; thus, their results were not reported in Figure 9.

Results in Figure 9 indicate that the modeled IP responses with the modified Fixman model agree remarkably well with simulations, showing that the modified model successfully captures both the dynamic process and magnitude of diffuse layer polarization. We also determined the enhanced permittivity $\Delta\varepsilon_{\text{eff}}$ and the characteristic time τ_c from both the simulated and modeled $\varepsilon_{\text{eff}} - f$ and $\sigma''_{\text{eff}} - f$ curves, and the results are shown in Figure 10 for all fluid salinities. It is clear that the variation trend of both $\Delta\varepsilon_{\text{eff}}$ and f_c with c_0 is consistent for simulation and theory. In addition, the absolute values match fairly well, as shown in Figure 10. This agreement provides additional evidence to support the applicability of the modified Fixman model.

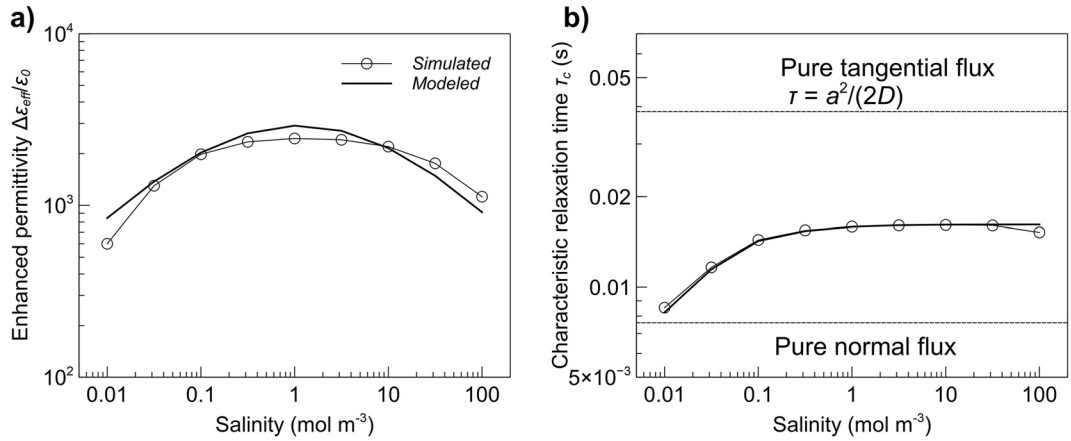

Figure 10. Salinity influence on (a) enhanced permittivity and (b) characteristic relaxation time of the diffuse layer polarization. The modeled results are from the modified Fixman model. Relaxation times from two limiting scenarios (pure tangential or normal ion movement in the diffuse layer) are also plotted in (b). The characteristic relaxation time of pure normal flux is calculated from the Dukhin-Shilov model.

Similarly, we also observe some discrepancies between modeling and simulation at high frequencies (e.g., ~100 kHz in Figure 9a). As mentioned in Section 5, this polarization has a length scale of several Debye lengths. Assume the charge separation is similar to that shown in Figure 6c, that is, about $3\kappa^{-1}$. We calculate the characteristic frequency of the polarization for all the salinities, and the results are shown in Figure 9 as vertical lines. It is found that the frequency of the simulated and calculated polarizations are consistent for $c_0 = 0.01$, 0.1, and 1 mol m^{-3}. For $c_0 = 0.01$, 0.1, and 1 mol m^{-3}, the characteristic frequency is higher than 10^7 Hz and is thus not shown in the figure. In general, the characteristic frequency is much larger than the primary polarization (~10 Hz), and it increases with the salinity (i.e., relaxation time $\tau \propto 1/c_0$; Chelidze & Gueguen, 1999). The agreement between simulation and modeling confirms that the polarization occurring outside the diffuse layer (regions 1 and 2 in Figure 1d) has a length scale on the order of Debye length. Although the contribution of this short-time polarization to the permittivity increment is negligible (Figure 9a), it does occur and has a much smaller length scale if compared to the grain size.

6.2. Mechanism of Salinity Effect

We explain the salinity effect of the enhanced permittivity $\Delta\varepsilon_{\text{eff}}$ and characteristic relaxation time τ_c using the local ion concentration perturbation information. Figure 10a shows that $\Delta\varepsilon_{\text{eff}}$ increases with salinity before reaching a maximum. This trend can be explained by the perturbation in ion concentrations within the diffuse layer (Figure 11). While the salinity increases from $c_0 = 0.01$ mol m^{-3} (Figure 11a) to $c_0 = 0.1$ mol m^{-3} (Figure 11b), the perturbation in Na^+ concentration in the diffuse layer (i.e., $x < \kappa^{-1}$) increases significantly as well. Given that the charge separation is constant (Figure 7a), the induced dipole moment will increase, leading to a higher degree of polarization and, thus, an increased $\Delta\varepsilon_{\text{eff}}$ (Figure 10a). However, when c_0 increases from 1 mol m^{-3} to 100 mol m^{-3}, Na^+ concentration perturbation in the diffuse layer decreases, as shown in Figure 11. Moreover, Cl^- concentrations perturbation also increases significantly. For instance, the concentration of Cl^- in the diffuse layer is negligible at $c_0 = 1$ mol m^{-3} (Figure 11b), but it increases to about one-third of Na^+ concentration perturbation. The presence of a significant amount of Cl^- in the diffuse layer further decreases the net charge amount contributing to the induced dipole moment, resulting in a decreased $\Delta\varepsilon_{\text{eff}}$ for $c_0 > 1$ mol m^{-3}, as shown in Figure 10a.

The characteristic relaxation time τ_c of diffuse layer polarization shows a clear dependence on the salinity (Figure 10b). To guide our analysis, we also plot the theoretical relaxation time of two limiting models, the Schwarz model (pure tangential ion flux) and the Dukhin-Shilov model (pure normal ion flux). While the relaxation time τ_c in the Schwarz model is $a^2/(2D)$, τ_c in the Dukhin-Shilov model is $a^2S/(2D)$, where S is a coefficient that accounts for the effects of fluid conductivity and additional grain conductivity due to ions in the diffuse layer (see Equation 34 in Bücker et al., 2019). As discussed, radial movement of counterions (and anions) during diffuse layer polarization requires ions to travel a short distance (on the order of κ^{-1}), but tangential ion movement is much longer, which is on the order of the grain radius a. Therefore, the time required to fully polarize

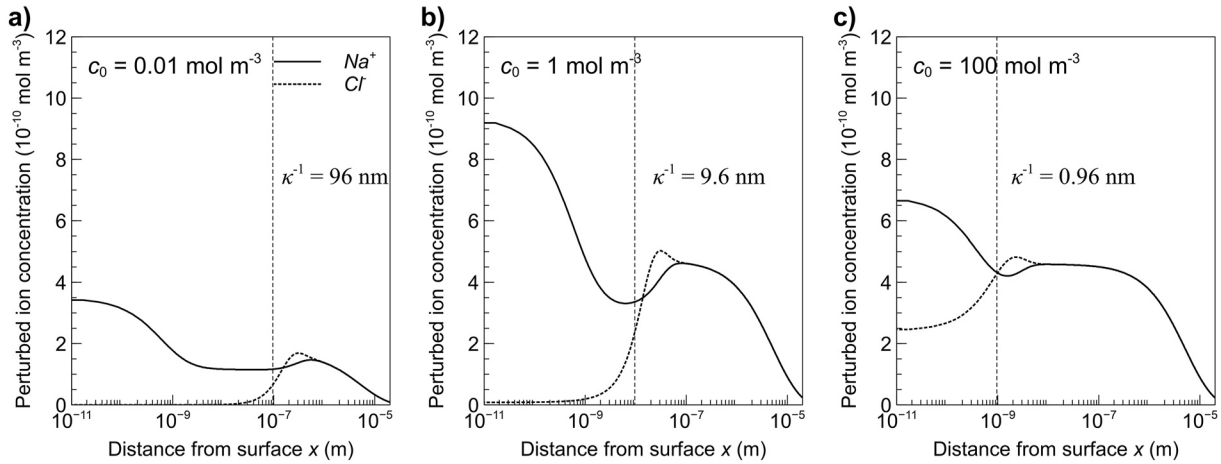

Figure 11. Perturbations in ion concentration within and outside of the diffuse layer of the grain-electrolyte system: (a) fluid salinity $c_0 = 0.01$ mol m^{-3}, (b) $c_0 = 1$ mol m^{-3}, and (c) $c_0 = 100$ mol m^{-3}. The Debye length κ^{-1} is also plotted in the figures.

the diffuse layer is longer for the case with pure tangential fluxes if compared to pure radial fluxes, as shown in Figure 10b.

At low salinities (e.g., $c_0 = 0.01$ mol m^{-3}), τ_c of diffuse layer polarization is close to the lower limit (Figure 10b), indicating the dominance of radial ion flux over tangential ion flux. To provide more evidence, we calculate both the tangential and normal Na^+ fluxes right next to the grain surface at 0.01 Hz (at which the diffuse layer has been fully polarized). The ratio of normal flux over tangential flux is plotted in Figure 12 for all the salinities. As shown in the figure, the ratio at $c_0 = 0.01$ mol m^{-3} is ~4,000, implying almost all Na^+ ions near the grain surface flow radially. This dominant normal flow gives a much shorter relaxation time, close to the lower limit calculated with the Dukhin-Shilov model (Figure 10b). The relaxation time τ_c increases with salinity until reaching a plateau (~0.017 s) when c_0 exceeds 10 mol m^{-3}. The increase in τ_c with salinity is consistent with the increased contribution of tangential Na^+ flux revealed in Figure 12. For instance, as c_0 increases from 0.01 to 10 mol m^{-3}, the ratio of radial flux over tangential flux decreases significantly, from ~4,000 to ~100. Because tangential Na^+ flux is associated with a longer travel distance, the time required to realize full polarization increases, as shown in Figure 10b. However, it should be noted that the total amount of ions moving normally still outweighs ions moving tangentially, even at high salinities. This is why the characteristic time at high c_0 is still much smaller than the limiting value calculated from the Schwarz model.

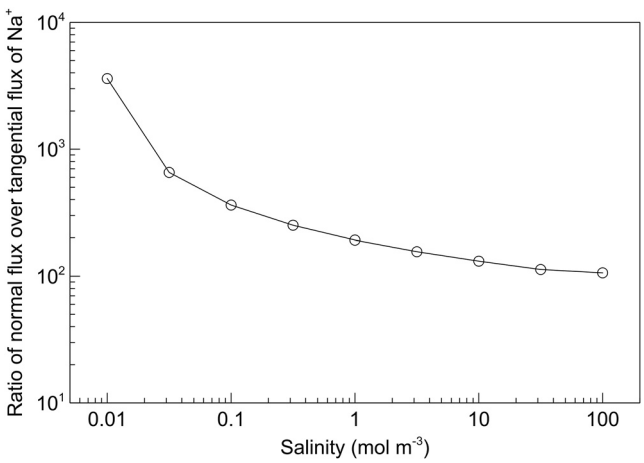

Figure 12. The ratio of the normal flux of Na^+ over the tangential flux of Na^+ in the diffuse layer right next to the grain surface. Overall, the normal flux of Na^+ dominates over tangential Na^+ flux, but its relative importance decreases with salinity.

6.3. Discussion

Many laboratory experimental data have shown that the imaginary conductivity of porous geological materials exhibits a non-monotonic variation with the pore fluid conductivity (Mendieta et al., 2021; Revil & Skold, 2011; Vinegar & Waxman, 1984; Weller et al., 2011). In general, the imaginary conductivity at a given frequency increases with the fluid conductivity (salinity) until reaching a maximum value; as the salinity further increases, the imaginary conductivity will decrease. This non-monotonic behavior has been observed in different types of materials such as clays (Mendieta et al., 2021; Vinegar & Waxman, 1984), sandstones (Revil & Skold, 2011; Weller et al., 2011), and unconsolidated sediments (Weller & Slater, 2012). These laboratory observations agree with the numerical results reported in Figure 10a. The observed increase in polarization with salinity at low water conductivity has been explained by the increased amount of counterions contributed to the EDL polarization (see Figures 10a and 10b or Niu, Revil, & Saidian, 2016; Revil & Skold, 2011). For the observed polarization decrease at high water conductivity, Mendieta et al. (2021) suggested that, at a particular salinity threshold, some polarization mechanisms (possibly membrane polarization)

cease to act. Our microscopic analysis highlighted the importance of coions (e.g., Cl^-) in EDL polarization at this high salinity range. Clearly, more work is still needed to better understand the mechanism behind this non-monotonic behavior.

The characteristic frequency or relaxation time of the EDL polarization has been found to depend weakly on the fluid salinity (e.g., Weller et al., 2011). Niu, Revil, and Saidian (2016) reported a general increase in relaxation time with salinity, which is consistent with the numerical results shown in Figure 10b. In Niu, Revil, and Saidian (2016), this salinity dependence was successfully modeled with a combination of Stern layer polarization and diffuse layer polarization (Lyklema et al., 1983; Niu & Revil, 2016); in essence, their modeling considers both tangential and radial movements of counterions as well as the exchanges between them. From this point of view, the theoretical modeling in Niu, Revil, and Saidian (2016) is consistent with our microscopic explanation in Figure 12. Both of them highlight the distinct contributions of tangential and radial ion movements to the relaxation time.

7. Conclusions

Numerical solutions of the Nernst-Planck-Poisson equations are used to study diffuse layer polarization of a spherical grain in NaCl electrolyte. Results confirm that the diffuse layer polarization results from the spatial separation between counterions and grain surface charges caused by an external electric field. This charge separation manifests itself as an enhanced permittivity if compared to the permittivity at high frequencies. Numerical results also show the radial movement of counterions outweighs tangential fluxes in the diffuse layer during the polarization. Though only a small fraction of counterions move tangentially, their contributions to the enhanced permittivity are much more significant than radial ion flux. This is because tangential ion flux in the diffuse layer induces a larger charge separation than the ion flux in the normal direction. The simulations also show that the ion concentration perturbations within the diffuse layer may also give rise to a concentration gradient in bulk solution right next to the diffuse layer. This concentration gradient, however, contributes negligibly to the enhanced permittivity.

Fluid salinity has a strong influence on diffuse layer polarization of the grain-electrolyte system. As salinity increases from low to intermediate values (e.g., <1 mol m^{-3}), the enhanced permittivity increases. This is because, at higher salinity, the external electric field could exert a larger perturbation in the counterion concentration in the diffuse layer, which increases the induced dipole moment and enhances permittivity. However, if the salinity increases further (e.g., >1 mol m^{-3}), perturbation in anion concentration in the diffuse layer becomes significant, canceling the effect of the perturbed counterion concentration. This results in a decreasing trend of induced dipole moment (and enhanced permittivity) with salinity. The fluid salinity also affects the time required to fully polarize the diffuse layer by changing the relative intensity of normal/tangential ion fluxes in the polarization. In general, the tangential movement of ions during polarization requires more time due to a longer travel distance. As the salinity increases, the ratio of normal ion flux over tangential flux decreases, and thus the associated relaxation time becomes longer.

The Schwarz model and the Dukhin-Shilvo model cannot accurately describe the IP responses of diffuse layer polarization because they only consider either the pure tangential or radial flux of counterions during polarization. Fixman model considers counterions movement in the diffuse layer along both directions, but it uses a single length parameter to define two disparate spatial regions (one for upscaling and one for ion exchange dynamics). The competing requirements of defining these two regions with this length parameter make the original Fixman model not suitable for modeling diffuse layer polarization. We modified the Fixman model to allow for two length parameters, and the proposed new model gives accurate predictions for both the shape and magnitude of the IP responses of the grain-electrolyte system over a broad salinity range.

Appendix A: Equations of the Modified Fixman Model

According to the Fixman model, the apparent complex conductivity $\overline{\sigma}_s^*$ of a charged sphere can be expressed as the function of its radius a (m), electrolyte concentration c_0 (mol m^{-3}), electrolyte conductivity σ_w (S m^{-1}), surface charge density Q_s (C m^{-2}), ion diffusion coefficient D (m^2 s^{-1}), and a length parameter R (m). If all the other parameters are given, $\overline{\sigma}_s^*$ is only a function of R, expressed as

$$\overline{\sigma}_s^*(R) = \frac{\sigma_w}{\frac{ac_0}{\rho_0} + \frac{\left[f(\lambda a) - \frac{g(\lambda R)}{g(-\lambda R)} f(-\lambda a)\right]}{g(\lambda a) - \frac{g(\lambda R)}{g(-\lambda R)} g(-\lambda a)}} \tag{A1}$$

where the parameter $\lambda = (1 + j)\sqrt{\omega/(2D)}$ and the functions $f(x)$ and $g(x)$ are expressed in Equations 9 and 10. The modified Fixman model for $\overline{\sigma}_s^*$ is then expressed as

$$\overline{\sigma}_s^* = \overline{\sigma}_s^*(+\infty) \frac{\max\left\{\text{imag}\left[\overline{\sigma}_s^*(a + \Delta)\right]\right\}}{\max\left\{\text{imag}\left[\overline{\sigma}_s^*(+\infty)\right]\right\}} \tag{A2}$$

where the small distance Δ (m) characterizes the region beyond the spherical grain that is used to upscale the complex surface conductance Σ_s^* (S) for determining the additional term $\Delta\sigma_s^*$ in apparent grain conductivity (Niu, Prasad, et al., 2016). In this study, $\Delta = 10\kappa^{-1}$ was used in the modeling.

Data Availability Statement

All the data used in this study are generated from Comsol models (Niu, 2022), which can be downloaded from https://doi.org/10.5281/zenodo.7261911.

Acknowledgments
Acknowledgment is made to the Donors of the American Chemical Society Petroleum Research Fund for financial support of this research. We thank the associated editor Dr. Max Moorkamp and two reviewers (Dr. Matthias Bücker and an anonymous one) for their constructive review comments, which have significantly improved the quality of a previous version of the manuscript. In particular, we are grateful to Dr. Bücker for sharing his Matlab code and Comsol model so that a comparison of previous study and this work is possible.

References

Attwa, M., & Günther, T. (2013). Spectral induced polarization measurements for predicting the hydraulic conductivity in sandy aquifers. *Hydrology and Earth System Sciences*, *17*(10), 4079–4094. https://doi.org/10.5194/hess-17-4079-2013

Bairlein, K., Bücker, M., Hördt, A., & Hinze, B. (2016). Temperature dependence of spectral induced polarization data: Experimental results and membrane polarization theory. *Geophysical Journal International*, *205*(1), 440–453. https://doi.org/10.1093/gji/ggw027

Bazant, M. Z., Thornton, K., & Ajdari, A. (2004). Diffuse-charge dynamics in electrochemical systems. *Physical Review E*, *70*(2), 021506. https://doi.org/10.1103/physreve.70.021506

Binley, A., Slater, L. D., Fukes, M., & Cassiani, G. (2005). Relationship between spectral induced polarization and hydraulic properties of saturated and unsaturated sandstone. *Water Resources Research*, *41*(12), W12417. https://doi.org/10.1029/2005wr004202

Börner, F. D., Schopper, J. R., & Weller, A. (1996). Evaluation of transport and storage properties in the soil and groundwater zone from induced polarization measurements. *Geophysical Prospecting*, *44*(4), 583–601. https://doi.org/10.1111/j.1365-2478.1996.tb00167.x

Brumleve, T. R., & Buck, R. P. (1978). Numerical solution of the Nernst-Planck and Poisson equation system with applications to membrane electrochemistry and solid state physics. *Journal of Electroanalytical Chemistry and Interfacial Electrochemistry*, *90*(1), 1–31. https://doi.org/10.1016/s0022-0728(78)80137-5

Bücker, M., Flores Orozco, A., & Kemna, A. (2018). Electrochemical polarization around metallic particles—Part 1: The role of diffuse-layer and volume-diffusion relaxation. *Geophysics*, *83*(4), E203–E217. https://doi.org/10.1190/geo2017-0401.1

Bücker, M., Flores Orozco, A., Undorf, S., & Kemna, A. (2019). On the role of Stern-and diffuse-layer polarization mechanisms in porous media. *Journal of Geophysical Research: Solid Earth*, *124*(6), 5656–5677. https://doi.org/10.1029/2019jb017679

Bücker, M., & Hördt, A. (2013). Analytical modelling of membrane polarization with explicit parametrization of pore radii and the electrical double layer. *Geophysical Journal International*, *194*(2), 804–813. https://doi.org/10.1093/gji/ggt136

Chelidze, T. L., & Gueguen, Y. (1999). Electrical spectroscopy of porous rocks: A review—I. Theoretical models. *Geophysical Journal International*, *137*(1), 1–15. https://doi.org/10.1046/j.1365-246x.1999.00799.x

Chen, J., Kemna, A., & Hubbard, S. S. (2008). A comparison between Gauss-Newton and Markov-Chain Monte Carlo–based methods for inverting spectral induced-polarization data for Cole-Cole parameters. *Geophysics*, *73*(6), F247–F259. https://doi.org/10.1190/1.2976115

Davis, C. A., Atekwana, E., Atekwana, E., Slater, L. D., Rossbach, S., & Mormile, M. R. (2006). Microbial growth and biofilm formation in geologic media is detected with complex conductivity measurements. *Geophysical Research Letters*, *33*(18), L18403. https://doi.org/10.1029/2006gl027312

Deceuster, J., & Kaufmann, O. (2012). Improving the delineation of hydrocarbon-impacted soils and water through induced polarization (IP) tomographies: A field study at an industrial waste land. *Journal of Contaminant Hydrology*, *136*, 25–42. https://doi.org/10.1016/j.jconhyd.2012.05.003

de Lima, O. A., & Sharma, M. M. (1992). A generalized Maxwell-Wagner theory for membrane polarization in shaly sands. *Geophysics*, *57*(3), 431–440. https://doi.org/10.1190/1.1443257

Eliaz, N., & Gileadi, E. (2019). *Physical electrochemistry: Fundamentals, techniques, and applications*. John Wiley & Sons.

Fixman, M. (1980). Charged macromolecules in external fields. I. The sphere. *The Journal of Chemical Physics*, *72*(9), 5177–5186. https://doi.org/10.1063/1.439753

Gazoty, A., Fiandaca, G., Pedersen, J., Auken, E., & Christiansen, A. V. (2012). Mapping of landfills using time-domain spectral induced polarization data: The Eskelund case study. *Near Surface Geophysics*, *10*(6), 575–586. https://doi.org/10.3997/1873-0604.2012046

Gurin, G., Titov, K., Ilyin, Y., & Tarasov, A. (2015). Induced polarization of disseminated electronically conductive minerals: A semi-empirical model. *Geophysical Journal International*, *200*(3), 1555–1565. https://doi.org/10.1093/gji/ggu490

Halisch, M., Hupfer, S., Weller, A., Dlugosch, R., & Plumhoff, H. P. (2018). An experimental setup for the assessment of effects of carbonate rock dissolution on complex electrical conductivity spectra. In *International Symposium of the Society of Core Analysts, Trondheim, Norway* (pp. 27–31).

Hashemi Amrei, S. M., Miller, G. H., Bishop, K. J., & Ristenpart, W. D. (2020). A perturbation solution to the full Poisson–Nernst–Planck equations yields an asymmetric rectified electric field. *Soft Matter*, *16*(30), 7052–7062. https://doi.org/10.1039/d0sm00417k

Hördt, A., Blaschek, R., Kemna, A., & Zisser, N. (2007). Hydraulic conductivity estimation from induced polarisation data at the field scale—The Krauthausen case history. *Journal of Applied Geophysics*, *62*(1), 33–46. https://doi.org/10.1016/j.jappgeo.2006.08.001

Jougnot, D., Ghorbani, A., Revil, A., Leroy, P., & Cosenza, P. (2010). Spectral induced polarization of partially saturated clay-rocks: A mechanistic approach. *Geophysical Journal International*, *180*(1), 210–224. https://doi.org/10.1111/j.1365-246x.2009.04426.x

Kemna, A., Binley, A., Cassiani, G., Niederleithinger, E., Revil, A., Slater, L., et al. (2012). An overview of the spectral induced polarization method for near-surface applications. *Near Surface Geophysics*, *10*(6), 453–468. https://doi.org/10.3997/1873-0604.2012027

Leroy, P., Revil, A., Kemna, A., Cosenza, P., & Ghorbani, A. (2008). Complex conductivity of water-saturated packs of glass beads. *Journal of Colloid and Interface Science*, *321*(1), 103–117. https://doi.org/10.1016/j.jcis.2007.12.031

Lesmes, D. P., & Morgan, F. D. (2001). Dielectric spectroscopy of sedimentary rocks. *Journal of Geophysical Research*, *106*(B7), 13329–13346. https://doi.org/10.1029/2000jb900402

Lyklema, J., Dukhin, S. S., & Shilov, V. N. (1983). The relaxation of the double layer around colloidal particles and the low-frequency dielectric dispersion: Part I. Theoretical considerations. *Journal of Electroanalytical Chemistry and Interfacial Electrochemistry*, *143*(1–2), 1–21. https://doi.org/10.1016/s0022-0728(83)80251-4

Macnae, J., & Hine, K. (2016). Comparing induced polarization responses from airborne inductive and galvanic ground systems: Tasmania. *Geophysics*, *81*(6), E471–E479. https://doi.org/10.1190/geo2016-0190.1

Marshall, D. J., & Madden, T. R. (1959). Induced polarization, a study of its causes. *Geophysics*, *24*(4), 790–816. https://doi.org/10.1190/1.1438659

Mendieta, A., Jougnot, D., Leroy, P., & Maineult, A. (2021). Spectral induced polarization characterization of non-consolidated clays for varying salinities—An experimental study. *Journal of Geophysical Research: Solid Earth*, *126*(4), e2020JB021125. https://doi.org/10.1029/2020jb021125

Mendieta, A., Maineult, A., Leroy, P., & Jougnot, D. (2023). Spectral induced polarization of heterogeneous non-consolidated clays. *Geophysical Journal International*, *233*(1), 436–447. https://doi.org/10.1093/gji/ggac466

Mitchell, J. K., & Soga, K. (2005). *Fundamentals of soil behavior* (Vol. 3). John Wiley & Sons.

Nelson, P. H., & van Voorhis, G. D. (1983). Estimation of sulfide content from induced polarization data. *Geophysics*, *48*(1), 62–75. https://doi.org/10.1190/1.1441408

Niu, Q. (2022). Revisiting the diffuse layer polarization of a spherical grain in electrolytes with numerical solutions of Nernst-Planck-Poisson equations (Version 1) [Dataset]. Zenodo. https://doi.org/10.5281/zenodo.7261911

Niu, Q., Prasad, M., Revil, A., & Saidian, M. (2016). Textural control on the quadrature conductivity of porous media. *Geophysics*, *81*(5), E297–E309. https://doi.org/10.1190/geo2015-0715.1

Niu, Q., & Revil, A. (2016). Connecting complex conductivity spectra to mercury porosimetry of sedimentary rocks. *Geophysics*, *81*(1), E17–E32. https://doi.org/10.1190/geo2015-0072.1

Niu, Q., Revil, A., & Saidian, M. (2016). Salinity dependence of the complex surface conductivity of the Portland sandstone. *Geophysics*, *81*(2), D125–D140. https://doi.org/10.1190/geo2015-0426.1

Niu, Q., & Zhang, C. (2018). Joint inversion of NMR and SIP data to estimate pore size distribution of geomaterials. *Geophysical Journal International*, *212*(3), 1791–1805. https://doi.org/10.1093/gji/ggx501

Niu, Q., Zhang, C., & Prasad, M. (2020). A framework for pore-scale simulation of effective electrical conductivity and permittivity of porous media in the frequency range from 1 mHz to 1 GHz. *Journal of Geophysical Research: Solid Earth*, *125*(10), e2020JB020515. https://doi.org/10.1029/2020jb020515

Nordsiek, S., & Weller, A. (2008). A new approach to fitting induced-polarization spectra. *Geophysics*, *73*(6), F235–F245. https://doi.org/10.1190/1.2987412

Okay, G., Leroy, P., Ghorbani, A., Cosenza, P., Camerlynck, C., Cabrera, J., et al. (2014). Spectral induced polarization of clay-sand mixtures: Experiments and modelingPolarization of clay-sand mixtures. *Geophysics*, *79*(6), E353–E375. https://doi.org/10.1190/geo2013-0347.1

Revil, A., Atekwana, E., Zhang, C., Jardani, A., & Smith, S. (2012). A new model for the spectral induced polarization signature of bacterial growth in porous media. *Water Resources Research*, *48*(9), W09545. https://doi.org/10.1029/2012wr011965

Revil, A., & Florsch, N. (2010). Determination of permeability from spectral induced polarization in granular media. *Geophysical Journal International*, *181*(3), 1480–1498. https://doi.org/10.1111/j.1365-246x.2010.04573.x

Revil, A., Florsch, N., & Camerlynck, C. (2014). Spectral induced polarization porosimetry. *Geophysical Journal International*, *198*(2), 1016–1033. https://doi.org/10.1093/gji/ggu180

Revil, A., Florsch, N., & Mao, D. (2015). Induced polarization response of porous media with metallic particles—Part 1: A theory for disseminated semiconductors. *Geophysics*, *80*(5), D525–D538. https://doi.org/10.1190/geo2014-0577.1

Revil, A., & Skold, M. (2011). Salinity dependence of spectral induced polarization in sands and sandstones. *Geophysical Journal International*, *187*(2), 813–824. https://doi.org/10.1111/j.1365-246x.2011.05181.x

Revil, A., Vaudelet, P., Su, Z., & Chen, R. (2022). Induced polarization as a tool to assess mineral deposits: A review. *Minerals*, *12*(5), 571. https://doi.org/10.3390/min12050571

Schroeder, P. (2018). *Clays in the critical zone*. Cambridge University Press.

Schwartz, N., & Furman, A. (2012). Spectral induced polarization signature of soil contaminated by organic pollutant: Experiment and modeling. *Journal of Geophysical Research*, *117*, B10203. https://doi.org/10.1029/2012jb009543

Schwarz, G. (1962). A theory of the low-frequency dielectric dispersion of colloidal particles in electrolyte solution. *The Journal of Physical Chemistry*, *66*(12), 2636–2642. https://doi.org/10.1021/j100818a067

Shilov, V. N., Delgado, A. V., Gonzalez-Caballero, F., & Grosse, C. (2001). Thin double layer theory of the wide-frequency range dielectric dispersion of suspensions of non-conducting spherical particles including surface conductivity of the stagnant layer. *Colloids and Surfaces A: Physicochemical and Engineering Aspects*, *192*(1–3), 253–265. https://doi.org/10.1016/s0927-7757(01)00729-4

Slater, L., Ntarlagiannis, D., Personna, Y. R., & Hubbard, S. (2007). Pore-scale spectral induced polarization signatures associated with FeS biomineral transformations. *Geophysical Research Letters*, *34*(21), L21404. https://doi.org/10.1029/2007gl031840

Slater, L., Ntarlagiannis, D., & Wishart, D. (2006). On the relationship between induced polarization and surface area in metal-sand and clay-sand mixtures. *Geophysics*, *71*(2), A1–A5. https://doi.org/10.1190/1.2187707

Šumi, F. (1961). The induced polarization method in ore investigation. *Geophysical Prospecting*, *9*(3), 459–477. https://doi.org/10.1111/j.1365-2478.1961.tb01524.x

Titov, K., Komarov, V., Tarasov, V., & Levitski, A. (2002). Theoretical and experimental study of time domain-induced polarization in water-saturated sands. *Journal of Applied Geophysics*, *50*(4), 417–433. https://doi.org/10.1016/s0926-9851(02)00168-4

Vinegar, H. J., & Waxman, M. H. (1984). Induced polarization of shaly sands. *Geophysics*, *49*(8), 1267–1287. https://doi.org/10.1190/1.1441755

Weller, A., Breede, K., Slater, L., & Nordsiek, S. (2011). Effect of changing water salinity on complex conductivity spectra of sandstones. *Geophysics*, *76*(5), F315–F327. https://doi.org/10.1190/geo2011-0072.1

Weller, A., & Slater, L. (2012). Salinity dependence of complex conductivity of unconsolidated and consolidated materials: Comparisons with electrical double layer models. *Geophysics*, *77*(5), D185–D198. https://doi.org/10.1190/geo2012-0030.1

Weller, A., Slater, L., Binley, A., Nordsiek, S., & Xu, S. (2015). Permeability prediction based on induced polarization: Insights from measurements on sandstone and unconsolidated samples spanning a wide permeability range. *Geophysics*, *80*(2), D161–D173. https://doi.org/10.1190/geo2014-0368.1

Wong, J. (1979). An electrochemical model of the induced-polarization phenomenon in disseminated sulfide ores. *Geophysics*, *44*(7), 1245–1265. https://doi.org/10.1190/1.1441005

Wu, C., Zou, C., Wu, T., Shen, L., Zhou, J., & Tao, C. (2021). Experimental study on the detection of metal sulfide under seafloor environment using time domain induced polarization. *Marine Geophysical Research*, *42*(2), 1–15. https://doi.org/10.1007/s11001-021-09438-w

Zhang, Z., Weller, A., & Kruschwitz, S. (2017). Pore radius distribution and fractal dimension derived from spectral induced polarization. *Near Surface Geophysics*, *15*(6), 625–632. https://doi.org/10.3997/1873-0604.2017035